nature geoscience

Article

https://doi.org/10.1038/s41561-025-01701-8

Global mangrove growth variability driven by climatic oscillation-induced sea-level fluctuations

Received: 4 June 2024

Accepted: 15 April 2025

Zhen Zhang[1,2] ✉, Xiangzhong Luo[3,4], Daniel A. Friess[2] & Yangfan Li[1] ✉

Mangroves are a carbon-dense and highly productive ecosystem but can experience massive dieback under environmental extremes. Climatic oscillations, such as the El Niño–Southern Oscillation (ENSO), are major drivers of global climate variability, yet their impact on mangrove growth at the global scale remains uncertain. Here, using long-term satellite observations from 2001 to 2020, we show that more than 50% of global mangrove areas experience significant variations during ENSO events, exhibiting a seesaw-like pattern across the Pacific Basin where mangrove leaf area decreases in the western Pacific but increases in the eastern Pacific during El Niño, with the reverse occurring during La Niña. The Indian Ocean Dipole affects mangroves across the Indian Ocean similarly but with a lower magnitude relative to ENSO. These patterns are driven by corresponding sea-level fluctuations across the Pacific and Indian ocean basins, with local contributions from lunar nodal cycles. Our study highlights the crucial role of short-term sea-level fluctuations driven by climatic oscillations in dominating the variability of coastal wetland growth and, consequently, in influencing the blue carbon sink.

Climatic oscillations, such as the El Niño–Southern Oscillation (ENSO)[1] and the Indian Ocean Dipole (IOD)[2], play a crucial role in driving the interannual variability of climate, including temperature, precipitation, wind and sea level[3]. Due to their intertidal location, mangrove forests, a highly productive coastal wetland widely distributed along tropical, subtropical and warm temperate coasts, are inherently exposed to the direct impacts of these oscillations[4]. Climatic oscillations can lead to extensive mangrove dieback, potentially transforming a blue carbon sink into a substantial carbon source[5]. Given the critical role of mangroves in providing a wide range of ecosystem services to coastal communities[6] and the anticipated increases in the frequency of major climatic oscillation modes[7,8], a comprehensive understanding of the response of mangroves to climatic oscillations, particularly given that mangroves may be more sensitive to climate variability than terrestrial forests[9], is essential to demonstrate their capacity to support coastal resilience and sustain their vital services.

Observational studies have underscored the vulnerability of mangroves to climatic extremes, including strong winds, drought, sea-level fluctuations and high temperatures, all of which can be triggered by climatic oscillations[10]. A notable example illustrating this vulnerability was the widespread mangrove dieback along a 1,000-km stretch of Northern Australia's Gulf of Carpentaria (GOC) during the 2015–2016 El Niño event[11]. However, our understanding of how mangrove forests respond to climatic oscillations has so far been largely limited to few field sites[12], predominantly along the coasts of Australia (for example, GOC, Kakadu National Park[13] and Mangrove Bay[14]). Indeed, extrapolating mangrove responses from specific regions to a global scale can be misleading, as climatic oscillations often result in different local

[1]State Key Laboratory of Marine Environmental Science, Key Laboratory of Coastal and Wetland Ecosystems (Ministry of Education), College of the Environment and Ecology, Xiamen University, Xiamen, China. [2]Department of Earth and Environmental Sciences, Tulane University, New Orleans, LA, USA. [3]Department of Geography, National University of Singapore, Singapore, Singapore. [4]Center for Nature-Based Climate Solutions, National University of Singapore, Singapore, Singapore. ✉e-mail: zzhang58@tulane.edu; yangf@xmu.edu.cn

climatic disturbances[15]. Even within these local sites, the role of climatic oscillations in driving mangrove dynamics remains under debate. Some studies attribute observed mangrove dieback to climatic anomalies caused by El Niño[16–18], while recent findings suggest that sea-level fluctuations associated with the lunar nodal cycle play a more important role in mangrove dynamics than El Niño[19]. Furthermore, aside from ENSO, other climatic oscillation modes, such as IOD, have been shown to strongly influence climatic and oceanographic factors in tropical and subtropical coasts[20,21], but their role in shaping the condition of mangrove forests remains poorly understood.

Our goal here is to examine the global-scale response of mangrove growth to ENSO and IOD events and to identify the driving factors behind these changes. To achieve this, we analyse anomalies in mangrove growth during ENSO and IOD events from 2001 to 2020, with a particular focus on three major events: the 2010–2012 La Niña, the 2015–2016 El Niño and the 2019 positive IOD (pIOD)[21], by using the 250-m-resolution Global LAnd Surface Satellite (GLASS) v6 monthly leaf area index (LAI) product[22] as an indicator of mangrove growth. To uncover the mechanisms driving the observed patterns, we perform a grid-scale analysis of coastal climatic and oceanographic forcing variations during these three events and quantify the contribution of each forcing factor to anomalies in mangrove growth. Finally, we assess the relative impacts of climatic oscillations and the lunar nodal cycle on sea-level fluctuations to determine their importance in driving mangrove growth anomalies under climatic oscillation events. Given our focus on variability, all presented analyses are based on monthly anomalies (detrended and deseasonalized data), unless otherwise specified.

Zonal seesaw-like pattern in mangrove anomaly

We assessed the temporal correlation between anomalies in mangrove growth and the magnitude of ENSO, as measured by the multivariate ENSO index (MEI), on a global scale. Mangrove leaf area exhibited a strong negative correlation with ENSO magnitude (Fig. 1a), with the most pronounced negative anomalies occurring during the 2015–2016 El Niño. By contrast, the most substantial positive anomalies were observed during the 2010–2012 La Niña. Changes in mangrove leaf area during ENSO events varied along the latitudinal gradient (Fig. 1b), with tropical mangroves experiencing more pronounced changes in the opposite direction compared with their northern counterparts. During the 2019 pIOD event, an extensive decline in mangrove LAI was observed, with widespread negative anomalies across regions south of 10° N (Fig. 1a,b).

Over 50% of global mangroves exhibited significant LAI variations ($P < 0.05$) in response to ENSO events (Fig. 2), while changes during neutral phases were minimal (Supplementary Fig. 1). Specifically, during the 2015–2016 El Niño, mangrove LAI declined in the western Pacific (Australia and Southeast Asia) and South America (Fig. 2a), with the most pronounced reduction occurring in the GOC, consistent with previous field studies[11,18]. This pattern contradicts terrestrial forests in tropical Asia and South America, which experienced a strong green-up due to increased shortwave radiation[23,24], implying the unique mechanisms of the responses of intertidal ecosystems to climatic perturbation[9]. Conversely, along eastern Pacific coasts (that is, western America; Extended Data Fig. 1), 48.3% of mangroves experienced significant growth enhancement during the same period (Fig. 2b). During the 2010–2012 La Niña, 42.9% of mangroves globally indicated a significantly positive response (Fig. 2c), especially in Australasia, where approximately 60% of mangroves experienced substantial LAI increases (Fig. 2d), while negative LAI anomalies were found predominantly in North America. This divergent pattern held across all ENSO events from 2001 to 2020 (Supplementary Fig. 2 and 3), with the exception of the weaker 2002–2003 El Niño, during which mangrove growth in the eastern Pacific was partially offset by localized degradation (Supplementary Fig. 2a). These results underscore a seesaw-like response along the Pacific Rim: during El Niño (La Niña), mangrove leaf area tends to increase (decrease) in the eastern Pacific while decreasing (increasing) in the western Pacific.

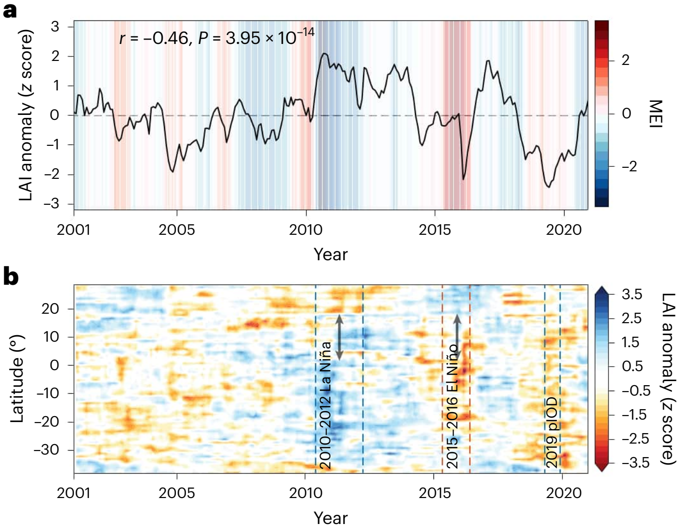

Fig. 1 | LAI anomaly in global mangroves during climatic events from 2001 to 2020. a, Temporal variations in monthly LAI anomaly (z score) over the global mangroves. The background shading shows the intensity of La Niña (blue) and El Niño (red) events defined by MEI. **b**, A Hovmöller diagram showing the LAI anomaly for each month and latitude. The vertical dashed lines mark the start and end of three climatic events.

This spatial pattern is further supported by correlations between mangrove LAI anomalies and ENSO intensity, quantified using MEI and the Oceanic Niño Index, which consistently show positive correlations in the eastern Pacific and negative correlations in the western Pacific (Supplementary Fig. 4). To assess the robustness of our global-scale findings at a local level, we analysed Landsat observations for two specific sites across the Pacific—Shoalwater Bay, Australia, and the Gulf of California, Mexico (Extended Data Fig. 2). The results indicate that mangroves in Shoalwater Bay (western Pacific) underwent widespread degradation, as indicated by a decreased Enhanced Vegetation Index (EVI), during the 2015–2016 El Niño event but exhibited growth enhancement during the 2010–2012 La Niña. By contrast, the mangroves in the Gulf of California (eastern Pacific) showed the opposite response pattern. These findings demonstrate that the seesaw response of mangrove growth to ENSO is robust across different methods of analysis, ENSO indices, satellite data sources and spatial–temporal scales.

Mangrove leaf area also shows a significant correlation with IOD, while no significant correlations were found with North Atlantic Oscillation and Southern Annular Mode, both globally and regionally (Supplementary Table 1). During the 2019 pIOD event, 17.8% of mangroves experienced significant decreases in LAI (Fig. 2e), particularly in Southeast Asia, western Australia and North America. By contrast, 15.3% of mangroves in East Africa experienced significant green-up (Fig. 2f), indicating a divergent response to the pIOD across the Indian Ocean Basin (Fig. 2e).

Our results are broadly supported by previous local-scale investigations that observed massive mangrove dieback or degradation due to ENSO or IOD, such as in GOC[11], Kakadu National Park[13], Mangrove Bay in Australia[17], Southeastern Brazil[25], Venezuela[26], Micronesia[27] and the Maldives[28], but also detect further signals beyond these local sites. For instance, previous local-scale studies have focused predominantly on the negative impacts of climatic oscillations on mangrove growth, while our findings reveal that mangroves can also experience green-up at the other side of ocean under climatic oscillations, as seen in the Gulf of California along the eastern Pacific during the 2015–2016 El Niño event. As such, extrapolating local-scale patterns to a global context may

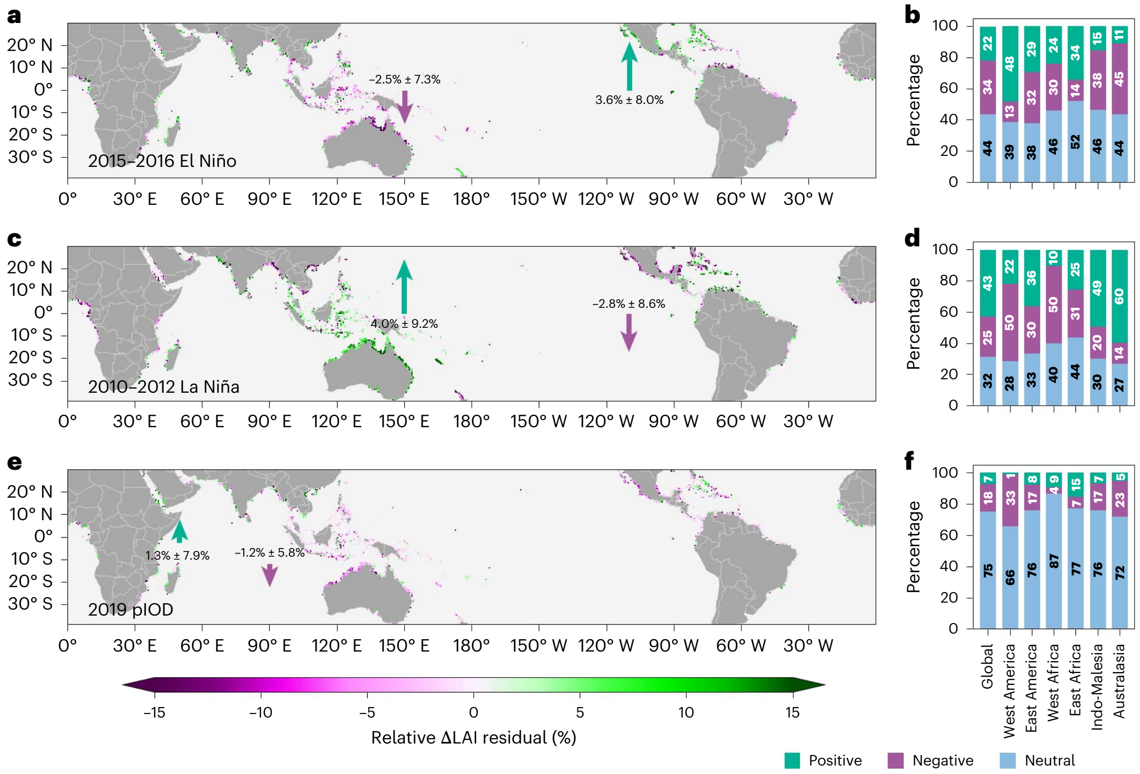

Fig. 2 | Zonal seesaw-like pattern of mangrove LAI anomaly corresponding to three climate oscillation events. **a**,**c**,**e**, LAI changes as a response to the 2015–2016 El Niño (**a**), 2010–2012 La Niña (**c**) and 2019 pIOD (**e**). **b**,**d**,**f**, The percentage of mangrove areas that exhibited a significantly increased LAI (green), a significantly decreased LAI (purple) or no significant difference with neutral phases in responding to the 2015–2016 El Niño (**b**), 2010–2012 La Niña (**d**) and 2019 pIOD (**f**). The spatial extent of the mangrove biogeographic region is shown in Extended Data Fig. 1. The downward directions represent a negative LAI anomaly, and the upward direction represents a positive LAI anomaly relative to corresponding neutral periods. In **a** and **c**, the right directions represent the eastern Pacific (that is, western America) and the left represent the western Pacific (120° E to 180° E). In **e**, the right directions represent the eastern Indian Ocean (77° E to 130° E) and the left directions represent the western Indian Ocean (25° E to 77° E).

overemphasize mangrove degradation while underestimating potential growth enhancement during climatic oscillations. Furthermore, our findings highlight the key role of the IOD in large-scale mangrove dynamics, a climatic oscillation mode that has been largely overlooked by previous studies focusing primarily on ENSO. Considering that Southeast Asia and Australia are influenced by both IOD and ENSO, our study suggests that mangroves in these regions, which constitute half of the global mangrove areas[29], are prone to frequent climate extremes.

Sea-level seesaw during ENSO and IOD

As variations in mangrove growth are generally associated with variations in climatic and oceanographic factors, we investigated the deviations of six key factors during each climatic event, encompassing three climatic variables: monthly mean air temperature (T_a), monthly mean wind speed (WS) and the Standardized Precipitation Evapotranspiration Index (SPEI), and three oceanic variables: monthly mean sea surface temperature (SST), sea surface salinity (SSS) and sea-level anomaly (SLA; measured as deviations from the long-term average in metres). To assess their deviations during climatic events, all variables were detrended, deseasonalized and subjected to z-score transformation, with the exception of SPEI, which inherently measures water availability anomalies[30] (Methods).

A widespread correlation between SLA and ENSO intensity was observed around the Pacific Rim, with a negative correlation in the western Pacific (that is, Southeast Asia and Australia) but a positive correlation in the eastern Pacific (that is, western America) (Fig. 3a). This suggests that, as the intensity of El Niño (positive MEI) increases, sea levels drop in the western Pacific but rise in the eastern Pacific. Indeed, we observed the divergent sea-level variations across the Pacific Basin during the 2015–2016 El Niño (Fig. 3c,d and Extended Data Fig. 3f), with a reversal occurring during the 2010–2012 La Niña (Fig. 3c,d and Extended Data Fig. 4f). Outside the Pacific, we did not observe significant correlations between SLA and ENSO (Fig. 3a).

SLA is also widely correlated with IOD intensity, along the Indian Ocean coast. We also observed a divergent signal: sea levels in the western Indian Ocean (that is, East Africa) rise with increasing pIOD (positive Dipole Mode Index (DMI)) intensity, while they fall in the eastern Indian Ocean (that is, South Asia and western Southeast Asia) (Fig. 3b,d and Extended Data Fig. 5f). The correlation between sea levels and IOD is stronger in the eastern Indian Ocean than the western Indian Ocean (Fig. 3b), while the correlation between sea levels and ENSO is comparable on both sides of the Pacific (Fig. 3a). In addition, the correlation between SLA and IOD is weaker than that between SLA and ENSO, indicating the stronger impacts of ENSO on sea levels than IOD (Fig. 3a,b). SLA due to climatic oscillations arises primarily from prevailing zonal wind anomalies over the tropical Pacific and Indian ocean basins[31], which affect seawater movement and result in the redistribution of seawater mass across the oceans[32,33].

Other climatic and oceanographic factors also showed strong variation during climatic events, but no clear seesaw-like patterns such as those seen in SLA were observed. Throughout the 2015–2016 El Niño, mangrove areas extensively experienced elevated T_a and SST, reduced water availability, intensified equatorial WS and heightened SSS (Extended Data Fig. 3 and Supplementary Fig. 5). By contrast, the 2010–2012 La Niña exhibited an opposite pattern, with cooler temperatures worldwide, enhanced water availability, weakened equatorial winds and decreased SSS (Extended Data Fig. 4 and Supplementary Fig. 5). Deviations in climatic and oceanic forcings were also evident

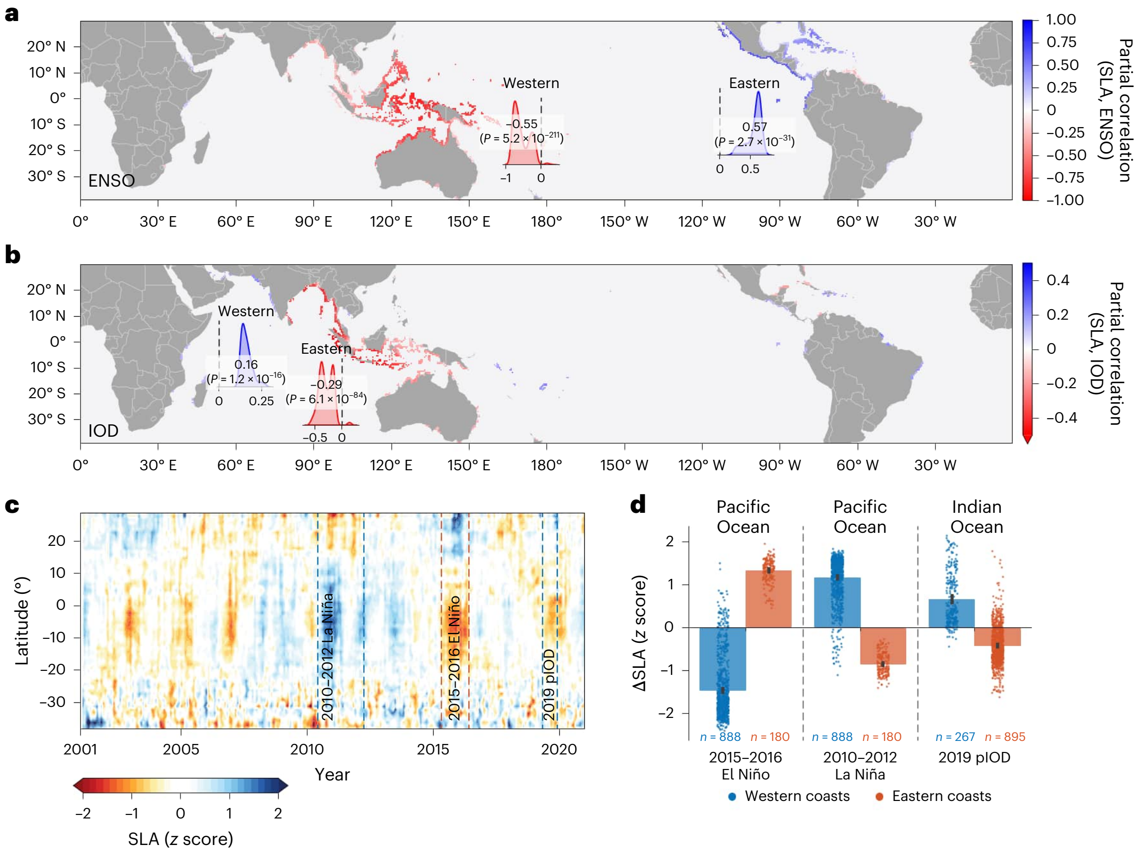

Fig. 3 | Relationships between SLA and climatic oscillations. **a**,**b**, Partial correlation between SLA and intensity of ENSO (**a**) and IOD (**b**), measured by MEI and DMI, respectively, after controlling for the effect of the other oscillation mode. Only significant grids ($P \leq 0.05$) are plotted. A probability density function of all significant grids belonging to each side is plotted. P values, derived from a two-sided Wilcoxon signed-rank test, reflect the significance of deviations from zero. **c**, Anomalies (z score) calculated over the period 2001–2020 for each latitude in mean monthly SLA. The vertical dashed lines mark the start and end of three climatic events. **d**, Average anomalies during the three extreme climatic events in SLA, with error bars showing the mean and 95% confidence intervals estimated using bootstrapping ($n = 1{,}000$). The western Pacific and the eastern Pacific in **a** and **d** refer to Indo-Malesia plus Australasia and western America, respectively (Extended Data Fig. 1). The eastern and the western Indian Ocean in **b** and **d** refer to areas between 77° E and 130° E and between 25° E and 77° E, respectively.

during the 2019 pIOD, although less pronounced than during ENSO (Supplementary Fig. 5). Over this period, mangroves in Southeast Asia experienced decreases in air and sea surface temperatures, except in the Philippines and Myanmar (Extended Data Fig. 5a,d). WS increased in Indonesia but remained relatively stable elsewhere (Extended Data Fig. 5c). SSS decreased in Africa and South America, contrasting with increases in North America, Malaysia and Sumatra (Extended Data Fig. 5e). Water availability displayed a seesaw pattern along the Indian Ocean (Supplementary Fig. 5g), characterized by increased SPEI on the western coasts but reduced SPEI on the eastern coasts (Extended Data Fig. 5b,f), leading to widespread drought conditions in the eastern Indian Ocean region during the 2019 pIOD (Extended Data Fig. 5b).

Anomalies in mangrove growth dominated by sea level

To assess the primary driver behind mangrove anomalies during climatic events, we separated the mangrove LAI responses to the 2015–2016 El Niño, 2010–2012 La Niña and 2019 pIOD into the individual contributions of each climatic and oceanic forcing, respectively. The contribution of each factor to LAI responses was determined by multiplying the sensitivity of LAI to the specific factor by the Δanomaly of that factor during each climatic event (Methods). The sum of these contributions represents the simulated LAI response to each climatic event, which aligns closely with both the spatial distribution and the magnitude of the satellite-observed anomaly in mangrove LAI (Supplementary Figs. 6 and 7). Factors that align with the direction of the satellite-observed ΔLAI anomaly (Fig. 2) and exhibit the highest magnitude are identified as the dominant factors at the grid scale (Fig. 4).

Sea-level variability during ENSO accounted for LAI anomalies in 33.8% (95% confidence interval 32.2–35.9%, determined by bootstrapping) of the global mangroves (Fig. 4). The seesaw-like pattern in LAI responses to ENSO can be effectively reconstructed solely from SLA (Extended Data Figs. 6 and 7), indicating that interannual fluctuation of tidal regimes shapes the fundamental pattern of mangrove leaf area responses to climatic oscillations. Our attribution unveils that the decline in mangrove LAI observed in the GOC during the 2015–2016 El Niño was primarily due to the decrease in sea level (Fig. 4a), consistent with earlier investigations based on field surveys and localized simulations[16,19]. Tide is a crucial water source for mangroves, and thus extremely low sea levels can lead to severe water deficits for arid/semi-arid mangroves where rainfall is scarce[34], resulting in massive dieback, as observed in the GOC. However, in humid regions like Southeast Asia, despite similar fallings in sea level during the 2015–2016 El Niño, we did not observe substantial mangrove dieback as in the GOC, suggesting that alternative freshwater sources probably buffer the effects of low sea levels[16]. This indicates that local environmental conditions can introduce spatial variability in how climatic oscillations impact mangroves.

Earlier research attributed the mangrove dieback in GOC to sea-level drops induced by the lunar nodal cycle[19]. By decomposing

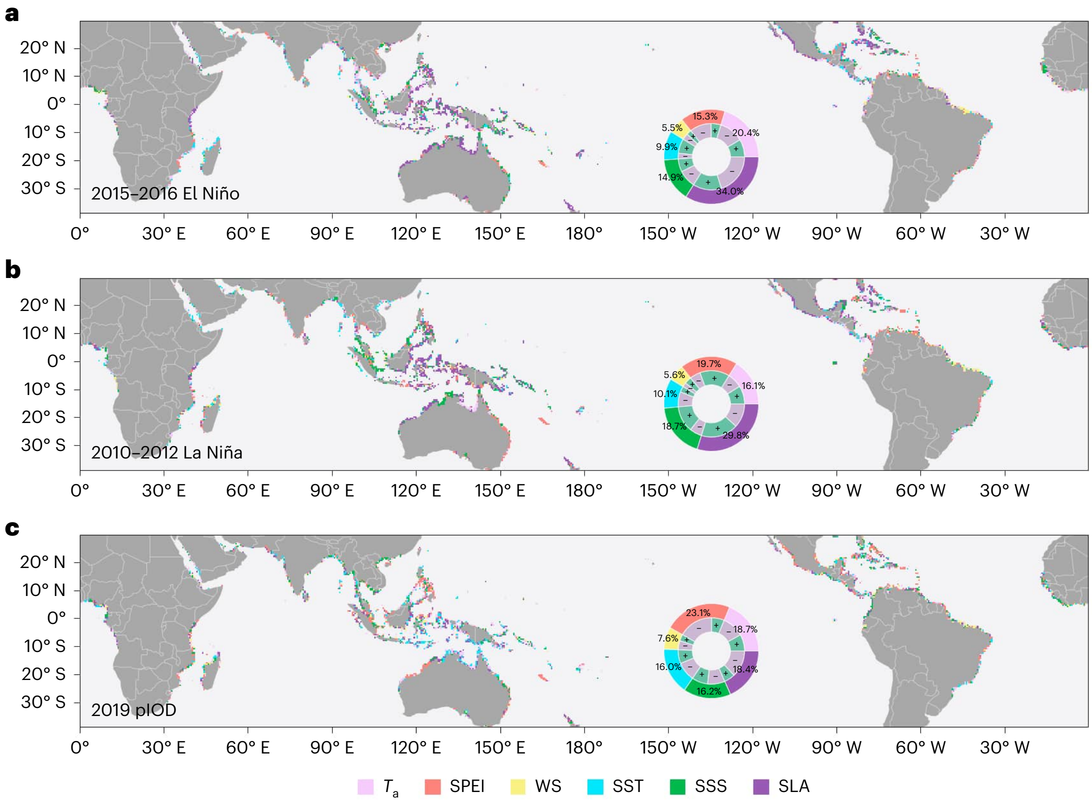

Fig. 4 | Attribution of mangrove LAI anomalies. a–**c**, The dominant factor driving responses of mangrove LAI to the 2015–2016 El Niño (**a**), 2010–2012 La Niña (**b**) and 2019 pIOD (**c**). The six contributors include mean monthly T_a, SPEI, WS, SST, SSS and SLA. The inset pie charts show the area fractions of mangroves dominated by each contributor. The 95% confidence interval for the area fractions of each contributor can be found in Supplementary Table 3. The ring embedded in the pie plot indicates the percentage of positive (green) and negative (purple) contribution.

sea-level variability into distinct components (Methods), we demonstrate that contributions from the nodal cycle are event and location specific (Extended Data Fig. 8). For the GOC area during the 2015–2016 El Niño, the sea-level drop was indeed driven more by the lunar nodal cycle than by El Niño (Extended Data Fig. 8a and Supplementary Fig. 8a,d). However, the nodal cycle made minimal contributions during the 2010–2012 La Niña and the 2019 pIOD events (Extended Data Fig. 8b,c). During the 2015–2016 period, sea levels in Southeast Asia and Northern Australia were influenced by both El Niño and the nodal cycle, with the latter dominating nearly half of the areas (Extended Data Fig. 8a). These results show that lunar nodal cycle does not consistently coincide with El Niño but can indeed contribute to decreasing sea levels where they do overlap.

While a sea-level seesaw was still evident across the Indian Ocean basin during the 2019 pIOD (95% confidence interval 16.9–20.0%, determined by bootstrapping), we found that water availability (SPEI) plays a more dominant role in the 2019 pIOD event, with the contribution of water availability to LAI anomalies exceeding 20% (95% confidence interval 21.6–24.9%) of mangrove areas (Fig. 4). The simulated contribution of water availability to LAI anomalies during the 2019 pIOD demonstrated a similar seesaw pattern, aligning with corresponding LAI anomalies and capturing the contrasting response across the Indian Ocean Basin (Extended Data Fig. 9b). The substantial mangrove LAI decreases along the western Australia were attributed to drought, and the positive LAI anomaly in the eastern Africa was a result of increased water availability, emphasizing the pronounced influence of pIOD-induced moisture changes on mangrove greenness.

The observed dominant roles of sea level and water availability are probably mediated through changes in pore water salinity[35], influencing mangrove physiological processes and consequently causing changes in mangrove leaf area. Variations in sea level can alter tidal inundation patterns, leading to reduced soil water immersion and increased exposure to air, which lowers soil moisture and elevates pore water salinity[14,36]. Under high salinity stress, certain mangrove species excrete more salt from their leaves and shed more leaves than usual to alleviate salt pressure[37], resulting in a reduction in leaf area. Elevated salinity also prompts mangroves to reduce stomatal conductance to mitigate water loss[38], leading to diminished carbon uptake and eventual dieback. In addition, reduced water input from tides and rainfall decreases soil moisture, further impeding water uptake by mangrove roots and heightening the risk of xylem embolism[39].The influence of other factors, including salinity, T_a, SST and WS, is generally minor or only locally significant. For example, during the 2015–2016 El Niño, strong winds contributed to a reduction in mangrove LAI in the Amazon estuary (Extended Data Fig. 6c), but the impacts of wind during the La Niña period were minimal, accounting for only 5.6% (95% confidence interval 4.7–6.5%, determined by bootstrapping) of areas without a clear spatial clustering (Fig. 4b).

Overall, this study reveals a zonal seesaw-like pattern in the response of mangrove growth to climatic oscillations across the Pacific and Indian ocean basins. With the anticipated increase in the frequency of El Niño and pIOD events[7,40], mangroves in Southeast Asia and Australia, particularly in arid/semi-arid areas, face a heightened risk of substantial dieback, which could potentially offset the increased productivity due to CO_2 fertilization and warming[9,41], introducing large uncertainty regarding the future benefits of ongoing mangrove conservation efforts. However, mangroves in these regions showed increased leaf area during La Niña events, suggesting that the future trajectory of mangrove growth depends on the frequency and phase of climate oscillation modes. Should La Niña events become more frequent and prolonged than El Niño, the greening trend in mangrove forests would probably intensify[9], reinforcing their role as a stable carbon sink. Monitoring short-term SLA and drought conditions, particularly in conjunction with more predictable lunar nodal cycles, could provide early warnings for mangroves at risk of climate-induced degradation. Together, our findings suggest that simulations of blue carbon ecosystems need to account for local impacts of climate oscillations, with particular attention to sea-level fluctuations.

Online content

Any methods, additional references, Nature Portfolio reporting summaries, source data, extended data, supplementary information, acknowledgements, peer review information; details of author contributions and competing interests; and statements of data and code availability are available at https://doi.org/10.1038/s41561-025-01701-8.

References

1. McPhaden, M. J., Zebiak, S. E. & Glantz, M. H. ENSO as an integrating concept in Earth science. *Science* **314**, 1740–1745 (2006).
2. Saji, N. H., Goswami, B. N., Vinayachandran, P. N. & Yamagata, T. A dipole mode in the tropical Indian Ocean. *Nature* **401**, 360–363 (1999).
3. Barber, R. T. & Chavez, F. P. Biological consequences of El Niño. *Science* **222**, 1203–1210 (1983).
4. Lovelock, C. E. & Reef, R. Variable impacts of climate change on blue carbon. *One Earth* **3**, 195–211 (2020).
5. Johannessen, S. C. & Christian, J. R. Why blue carbon cannot truly offset fossil fuel emissions. *Commun. Earth Environ.* **4**, 411 (2023).
6. Worthington, T. A. et al. Harnessing big data to support the conservation and rehabilitation of mangrove forests globally. *One Earth* **2**, 429–443 (2020).
7. Cai, W. et al. Increasing frequency of extreme El Niño events due to greenhouse warming. *Nat. Clim. Change* **4**, 111–116 (2014).
8. Cai, W. et al. Increased frequency of extreme La Niña events under greenhouse warming. *Nat. Clim. Change* **5**, 132–137 (2015).
9. Zhang, Z. et al. Stronger increases but greater variability in global mangrove productivity compared to that of adjacent terrestrial forests. *Nat. Ecol. Evol.* **8**, 239–250 (2024).
10. Friess, D. A., Adame, M. F., Adams, J. B. & Lovelock, C. E. Mangrove forests under climate change in a 2 °C world. *Wiley Interdiscip. Rev. Clim. Change* **13**, e792 (2022).
11. Duke, N. C. et al. Large-scale dieback of mangroves in Australia. *Mar. Freshw. Res.* **68**, 1816–1829 (2017).
12. Sippo, J. Z., Lovelock, C. E., Santos, I. R., Sanders, C. J. & Maher, D. T. Mangrove mortality in a changing climate: an overview. *Estuar. Coast. Shelf Sci.* **215**, 241–249 (2018).
13. Asbridge, E. F. et al. Assessing the distribution and drivers of mangrove dieback in Kakadu National Park, northern Australia. *Estuar. Coast. Shelf Sci.* **228**, 106353 (2019).
14. Lovelock, C. E., Feller, I. C., Reef, R., Hickey, S. & Ball, M. C. Mangrove dieback during fluctuating sea levels. *Sci. Rep.* **7**, 1680 (2017).
15. Timmermann, A. et al. El Niño–Southern Oscillation complexity. *Nature* **559**, 535–545 (2018).
16. Duke, N. C. et al. ENSO-driven extreme oscillations in mean sea level destabilise critical shoreline mangroves—an emerging threat. *PLoS Clim.* **1**, e0000037 (2022).
17. Hickey, S. M. et al. ENSO feedback drives variations in dieback at a marginal mangrove site. *Sci. Rep.* **11**, 8130 (2021).
18. Abhik, S. et al. Influence of the 2015–2016 El Niño on the record-breaking mangrove dieback along northern Australia coast. *Sci. Rep.* **11**, 20411 (2021).
19. Saintilan, N. et al. The lunar nodal cycle controls mangrove canopy cover on the Australian continent. *Sci. Adv.* **8**, eabo6602 (2022).
20. Palmer, P. I. et al. Drivers and impacts of Eastern African rainfall variability. *Nat. Rev. Earth Environ.* **4**, 254–270 (2023).
21. Ratna, S. B., Cherchi, A., Osborn, T. J., Joshi, M. & Uppara, U. The extreme positive Indian Ocean Dipole of 2019 and associated Indian summer monsoon rainfall response. *Geophys. Res. Lett.* **48**, e2020GL091497 (2021).
22. Ma, H. & Liang, S. Development of the GLASS 250-m leaf area index product (version 6) from MODIS data using the bidirectional LSTM deep learning model. *Remote Sens. Environ.* **273**, 112985 (2022).
23. Satriawan, T. W. et al. Strong green-up of tropical Asia during the 2015/16 El Niño. *Geophys. Res. Lett.* **51**, e2023GL106955 (2024).
24. Janssen, T. et al. Drought effects on leaf fall, leaf flushing and stem growth in the Amazon forest: reconciling remote sensing data and field observations. *Biogeosciences* **18**, 4445–4472 (2021).
25. Servino, R. N., Gomes, L. E., de, O. & Bernardino, A. F. Extreme weather impacts on tropical mangrove forests in the Eastern Brazil Marine Ecoregion. *Sci. Total Environ.* **628–629**, 233–240 (2018).
26. Otero, X. L. et al. High fragility of the soil organic C pools in mangrove forests. *Mar. Pollut. Bull.* **119**, 460–464 (2017).
27. Drexler, J. Z. & Ewel, K. C. Effect of the 1997–1998 ENSO-related drought on hydrology and salinity in a micronesian wetland complex. *Estuaries* **24**, 347–356 (2001).
28. Carruthers, L. et al. Sea-level rise and extreme Indian Ocean Dipole explain mangrove dieback in the Maldives. *Sci. Rep.* **14**, 27012 (2024).
29. Bunting, P. et al. The Global Mangrove Watch—a new 2010 global baseline of mangrove extent. *Remote Sens.* **10**, 1669 (2018).
30. Slette, I. J. et al. How ecologists define drought, and why we should do better. *Glob. Change Biol.* **25**, 3193–3200 (2019).
31. Vecchi, G. A. et al. Weakening of tropical Pacific atmospheric circulation due to anthropogenic forcing. *Nature* **441**, 73–76 (2006).
32. Merrifield, M. A., Thompson, P. R. & Lander, M. Multidecadal sea level anomalies and trends in the western tropical Pacific. *Geophys. Res. Lett.* **39**, L13602 (2012).
33. Widlansky, M. J., Timmermann, A. & Cai, W. Future extreme sea level seesaws in the tropical Pacific. *Sci. Adv.* **1**, e1500560 (2015).
34. Adame, M. F. et al. Mangroves in arid regions: ecology, threats, and opportunities. *Estuar. Coast. Shelf Sci.* **248**, 106796 (2021).
35. Zhu, X., Sun, C. & Qin, Z. Drought-induced salinity enhancement weakens mangrove greenhouse gas cycling. *J. Geophys. Res. Biogeosci.* **126**, e2021JG006416 (2021).
36. Bathmann, J. et al. Modelling mangrove forest structure and species composition over tidal inundation gradients: the feedback between plant water use and porewater salinity in an arid mangrove ecosystem. *Agric. Meteorol.* **308–309**, 108547 (2021).
37. Hoppe-Speer, S. C. L., Adams, J. B., Rajkaran, A. & Bailey, D. The response of the red mangrove *Rhizophora mucronata* Lam. to salinity and inundation in South Africa. *Aquat. Bot.* **95**, 71–76 (2011).
38. Ball, M. C. & Farquhar, G. D. Photosynthetic and stomatal responses of two mangrove species, *Aegiceras corniculatum* and *Avicennia marina*, to long term salinity and humidity conditions. *Plant Physiol.* **74**, 1–6 (1984).
39. Méndez-Alonzo, R., López-Portillo, J., Moctezuma, C., Bartlett, M. K. & Sack, L. Osmotic and hydraulic adjustment of mangrove saplings to extreme salinity. *Tree Physiol.* **36**, 1562–1572 (2016).

40. Wang, J. et al. Modulation of land photosynthesis by the Indian Ocean Dipole: satellite-based observations and CMIP6 future projections. *Earth Future* **9**, e2020EF001942 (2021).
41. Ruehr, S. et al. Evidence and attribution of the enhanced land carbon sink. *Nat. Rev. Earth Environ.* **4**, 518–534 (2023).

Methods

Mangrove area dataset

As our focus was on detecting anomalous mangrove leaf area resulting from climatic oscillations, we confined the study area to undisturbed global mangrove areas from 2001 to 2020, as per previous studies[9]. Undisturbed mangroves were defined as areas with no detected land-cover changes between 2001 and 2020, to eliminate interannual area fluctuations caused by human activities (for example, land-cover conversion for commodity production) and large-scale natural drivers of mangrove area change, such as shoreline erosion[42]. Specifically, we initially extracted intersecting areas from the Global Mangrove Watch v3 mangrove distribution data between 1996 (the closest year available in Global Mangrove Watch v3 data to 2001) and 2020 as the undisturbed mangrove regions[43]. Temporal changes in mangrove area between the 2 years (for example, degradation followed by recovery) are preserved in our analysis through this 2-year intersecting process. This resulted in a final global area of 133,559.5 km^2, or 87.5% of the global mangrove area in 1996. Subsequently, we quantified the proportion of mangroves within each 250-m GLASS LAI pixel, retaining only those pixels with over 80% mangrove cover to eliminate uncertainties arising from mixed pixels. The results from the 80% coverage threshold align closely with those obtained from higher-resolution Landsat data at the local scale (Extended Data Fig. 2). Furthermore, we tested additional coverage thresholds, including 0% and 60%, and found that the observed seesaw pattern in mangrove growth response to ENSO events remained consistent across these thresholds (Extended Data Fig. 2). In the end, 1,415,320 pixels at the 250-m resolution were retained as the final mangrove area for our analysis.

Mangrove LAI data

LAI (unit: m^2 m^{-2}) is defined as the one-sided green leaf area per unit ground area for broad-leaved vegetation such as mangroves[44]. Changes in leaf area, both reductions (leaf shedding) and increases, impact vegetation productivity[45], making it a key variable in carbon cycle studies. Analysing mangrove LAI requires the use of fine-resolution, temporally seamless data, given their fragmented distribution pattern and frequent exposure to tidal inundation and cloud cover[46]. While the widely used Landsat archive offers 30-m-resolution data dating back to 1984, its relatively low revisit frequency of 16 days restricts its ability to deliver continuous spatiotemporal data for mangroves. For example, in July 2010, when the La Niña event reached its peak intensity between 2001 and 2020, Landsat images showed large data gaps due to cloud cover, a limited number of available images, and scan line issues associated with Landsat 7 (Supplementary Fig. 9). By contrast, Moderate Resolution Imaging Spectroradiometer (MODIS) provides higher temporal resolution, enabling more continuous monitoring of mangrove dynamics. However, MODIS products, while offering a variety of vegetation functional parameters, are constrained by coarser spatial resolutions of 500–1,000 m (ref. 47), which are insufficient for studying ecosystems with patchy distributions such as mangroves. To address this limitation, the GLASS LAI version 6 product uses spatial downscaling techniques, integrating existing coarse-resolution LAI data with 250-m-resolution MODIS spectral reflectance bands, resulting in the first global LAI product at the 250-m resolution. Moreover, these data use a time-series deep learning model trained on each pixel to reconstruct surface reflectance time series every 2 years, so that data gaps resulting from cloud cover and fluctuations in vegetation greenness due to tidal inundation could be addressed. This generates a spatio-temporally seamless dataset[22], making it particularly suitable for mangrove research. The dataset has been validated, proving effective even at the flux tower scale for mangroves[48]. GLASS LAI data are provided as an 8-day composite and were resampled to monthly means to align with the temporal sampling of climatic and oceanic forcing data.

Climatic and oceanic forcing data

This study incorporates six potential factors into the attribution model, encompassing both climate and oceanic aspects. While traditional climate indicators such as precipitation and vapour pressure deficit were not included due to their primary reflection of humidity changes[49], this aspect is effectively captured by the SPEI, an ecologically relevant metric specifically designed to quantify drought severity[50]. Monthly average data were extracted for the following variables: T_a (unit: °C), SPEI (unitless), WS (unit: m s^{-1}), SST (unit: °C), SSS (measured in practical salinity units, PSU) and SLA (unit: m).

T_a and WS data were obtained from Modern-Era Retrospective analysis for Research and Applications v.2 (MERRA-2) monthly climate products at a 0.5° × 0.625° resolution[51]. SPEI data were obtained from the global SPEI version 2.7 dataset[52], provided at a spatial resolution of 0.5° globally, covering the period from 1901 to 2020 on a monthly basis. SPEI represents a *z*-score-standardized value, indicating the extent of deviation from the multiyear average water balance, with smaller values indicating more severe moisture deficiency[30]. The calculation of SPEI requires the specification of a time window. Thus, we conducted an analysis to determine the correlation between SPEI and mangrove LAI for varying time windows ranging from 1 to 12 months. It was observed that SPEI calculated on the basis of a 4-month time window exhibited the highest correlation with mangrove LAI (Supplementary Fig. 10). Consequently, SPEI4 data were selected for subsequent analyses.

SST data were sourced from the Multi Observation Global Ocean ARMOR3D L4 dataset[53], available at a resolution of 0.25°. This dataset provides sea water temperature at various depths, with the temperature at the 0-m depth selected to represent SST. SSS was obtained from Global Ocean Physics Reanalysis version 1 (GLORYS12V1) product, which provides global monthly gap-free SSS data at a resolution of 0.125°. This dataset integrates data from multiple satellite sources, including the National Aeronautics and Space Administration (NASA)'s Soil Moisture Active Passive (SMAP) and ESA's Soil Moisture Ocean Salinity (SMOS) satellites, along with in situ salinity measurements. Data on SLA were acquired at a resolution of 0.25° from the Copernicus Marine Environment Monitoring Service satellite altimetry measurements. Here, SLA represents the difference between monthly average sea surface height and the 20-year average between 1993 and 2012. As the climatic and oceanic data cover only oceanic regions, with gaps in some mangrove areas, nearshore values were extrapolated to land using a 5 × 5 mean filter to overlay with the mangrove extent[54]. All datasets analysed in this study were harmonized to a common 0.5° grid to ensure consistency in spatial resolutions. Details of all datasets used in the analysis are given in Supplementary Table 2.

Anomalies in mangrove growth and climate during three oscillation events

For all datasets used in our analysis, we removed the long-term linear trend for each 0.5° grid, and the seasonal fluctuations were also removed by subtracting the monthly mean seasonal climatology so that our focus was on the interannual variability[55]. It is worth noting that, for SPEI, which inherently measures anomaly in water availability, neither detrending nor deseasonalization was required. What remains after detrending and deseasonalizing (the residual time series) is the variation reflecting the response of the variable to stochastic disturbance. This variation was converted to *z* scores to quantify anomaly. A visual representation of this process is shown Supplementary Fig. 11.

We used the MEI to determine the occurrence of El Niño and La Niña events, where El Niño was defined as MEI exceeding 0.5 persisting for a consecutive 3-month period and La Niña as MEI falling below 0.5 persisting for three consecutive months. The DMI was utilized to measure the intensity of the IOD, with pIOD events identified as DMI equal to or greater than 0.52 for at least three consecutive months[56]. The 2019 pIOD event is particularly noteworthy as it occurred without a simultaneous El Niño event in the Pacific, providing a unique opportunity to separate their individual impacts[40]. Consequently, we delineated the period of the 2015–2016 El Niño event from May 2015 to May 2016, the period of the 2010–2012 La Niña event from June 2010 to March 2012 and the period of the 2019 pIOD event from May 2019 to November 2019. Two other climatic oscillation modes—North Atlantic Oscillation and Southern Annular Mode—were also tested for their potential impacts on mangroves[55].

For each oscillation event, we defined a neutral time window to act as a baseline for assessing the normal state of the mangroves. This window encompasses the months before the oscillation, with MEI values ranging from −0.5 to 0.5 and DMI values between −0.52 and 0.52. For instance, the neutral phase for the 2015–2016 El Niño refers to those months between March 2012 (after the end of La Niña) and May 2015 (before the start of El Niño) with weak MEI or DMI signals. We choose to use the intervals between climate oscillation events as neutral phases, rather than all neutral months throughout the study period, to avoid including periods when mangroves may not have fully recovered from previous oscillations, which could result in a persistently low LAI. This approach prevents the misidentification of anomalies in subsequent events, such as the 2019 pIOD.

The difference in the average anomaly (that is, *z* score) between each extreme climatic event and its corresponding neutral phase was defined as the anomaly induced by climatic oscillations (denoted as Δanomaly). In addition, we calculated the relative anomaly to quantify the changes in mangrove LAI during the three climatic extreme events. This was measured as the average deviation of LAI residuals ($\mathrm{LAI}_{\mathrm{residual}}^{\mathrm{ENSO/IOD}} - \mathrm{LAI}_{\mathrm{residual}}^{\mathrm{Neutral}}$) during the extreme events relative to the average LAI during neutral phases ($\mathrm{LAI}^{\mathrm{Neutral}}$; serving as the baseline LAI under normal conditions), expressed as the percentage change in LAI (denoted as relative ΔLAI anomaly)

$$\text{Relative } \Delta\text{LAI anomaly} = \frac{\mathrm{LAI}_{\mathrm{residual}}^{\mathrm{ENSO/IOD}} - \mathrm{LAI}_{\mathrm{residual}}^{\mathrm{Neutral}}}{\mathrm{LAI}^{\mathrm{Neutral}}}. \tag{1}$$

We performed independent *t*-tests to assess the statistical significance of the relative ΔLAI anomaly and Δanomaly for each grid cell, with the null hypothesis that the average anomaly during climatic events is equivalent to that during neutral phases. The sample sizes were $N = 22$ for the 2010–2012 La Niña phase, $N = 13$ per grid for the 2015–2016 El Niño phase and $N = 7$ for the 2019 pIOD. Corresponding sample sizes for the neutral phases were $N = 46$ for the 2010–2012 La Niña, $N = 31$ for the 2015–2016 El Niño and $N = 21$ for the 2019 pIOD.

Nodal cycle modulation

We decomposed SLA data from satellite altimetry into two components: contributions from lunar nodal cycles and climatic oscillations. This separation was performed to specifically quantify the impact of climate oscillations on SLA. To achieve this, we applied a regression model to the monthly SLA, enabling us to estimate fluctuations in sea level induced by nodal cycles for each 0.5° grid[57,58]

$$\begin{aligned}\mathrm{SLA}(t) = \beta_0 + \beta_1 \cos\left(\frac{2\pi}{4.4}t\right) + \beta_2 \sin\left(\frac{2\pi}{4.4}t\right) + \beta_3 \cos\left(\frac{2\pi}{18.61}t\right)\\ + \beta_4 \sin\left(\frac{2\pi}{18.61}t\right) + \varepsilon,\end{aligned} \tag{2}$$

where SLA(t) represents the monthly SLA at time t after detrending and deseasonalization. The parameter β_0 is the intercept, β_1 and β_2 are the amplitudes of the 4.4-year perigean subharmonic, β_3 and β_4 are the amplitudes of the 18.61-year lunar nodal cycle, and ε denotes the model residual. We used the ordinary least-squares technique to estimate the coefficients β_1 to β_4 and calculated the nodal cycle contribution to SLA by summing the effects of the 4.4-year perigean subharmonic and the 18.61-year lunar nodal cycle. The discrepancy between the observed SLA and the simulated SLA derived from nodal contributions was defined as the climatic oscillation-induced SLA for each event.

Attribution analysis

At each grid cell, we attributed the detected mangrove LAI anomaly during each extreme climatic event to climatic and oceanic forcings using a regression model. We first quantified the sensitivity of mangrove LAI to each forcing variable by fitting a multiple linear regression model, expressed as[59]

$$\begin{aligned}\mathrm{LAI} &= \frac{\partial \mathrm{LAI}}{\partial T_a} T_a + \frac{\partial \mathrm{LAI}}{\partial \mathrm{SPEI}} \mathrm{SPEI} + \frac{\partial \mathrm{LAI}}{\partial \mathrm{WS}} \mathrm{WS}\\ &\quad + \frac{\partial \mathrm{LAI}}{\partial \mathrm{SST}} \mathrm{SST} + \frac{\partial \mathrm{LAI}}{\partial \mathrm{SSS}} \mathrm{SSS} + \frac{\partial \mathrm{LAI}}{\partial \mathrm{SLA}} \mathrm{SLA} + \varepsilon,\\ &= \gamma_{\mathrm{LAI}}^{T_a} T_a + \gamma_{\mathrm{LAI}}^{\mathrm{SPEI}} \mathrm{SPEI} + \gamma_{\mathrm{LAI}}^{\mathrm{WS}} \mathrm{WS} + \gamma_{\mathrm{LAI}}^{\mathrm{SST}} \mathrm{SST}\\ &\quad + \gamma_{\mathrm{LAI}}^{\mathrm{SSS}} \mathrm{SSS} + \gamma_{\mathrm{LAI}}^{\mathrm{SLA}} \mathrm{SLA} + \varepsilon\end{aligned} \tag{3}$$

where LAI, T_a, WS, SST, SSS and SLA are all *z*-transformed anomaly time series; the slope of each variable represents the sensitivity (γ) of mangrove LAI to each variable and is computed using the ordinary least-squares method; and ε is the model residual, representing the total error in modelling time-series LAI for each grid. Furthermore, LAI anomaly during each extreme climatic event could be expressed as

$$\begin{aligned}\Delta\mathrm{LAI} = \gamma_{\mathrm{LAI}}^{T_a} \Delta T_a + \gamma_{\mathrm{LAI}}^{\mathrm{SPEI}} \Delta\mathrm{SPEI} + \gamma_{\mathrm{LAI}}^{\mathrm{WS}} \Delta\mathrm{WS} + \gamma_{\mathrm{LAI}}^{\mathrm{SST}} \Delta\mathrm{SST}\\ + \gamma_{\mathrm{LAI}}^{\mathrm{SSS}} \Delta\mathrm{SSS} + \gamma_{\mathrm{LAI}}^{\mathrm{SLA}} \Delta\mathrm{SLA} + \varepsilon,\end{aligned} \tag{4}$$

where Δ denotes the variable difference between ENSO or IOD event and neutral phases. Each term in equation (4) indicates contributions to ΔLAI[60] (Extended Data Figs. 6–8). The primary driver of ΔLAI for each extreme climatic event was then determined as the forcing factor with greatest contribution as well as the same sign of ΔLAI (that is, both positive or both negative).

Data availability

All data used in this study are publicly available. The GLASS V6 LAI data are available at http://www.glass.umd.edu/LAI/MODIS/250m/. The Global Mangrove Watch v3.0 data are available via Zenodo at https://doi.org/10.5281/zenodo.6894273 (ref. 61). Gridded climate data used in this study are presented in Supplementary Table 2.

Code availability

All code used in this study is available from the corresponding authors upon reasonable request.

References

42. Goldberg, L., Lagomasino, D., Thomas, N. & Fatoyinbo, T. Global declines in human-driven mangrove loss. *Glob. Change Biol.* **26**, 5844–5855 (2020).
43. Bunting, P. et al. Global mangrove extent change 1996–2020: Global Mangrove Watch Version 3.0. *Remote Sens.* **14**, 3657 (2022).
44. Kamal, M., Phinn, S. & Johansen, K. Assessment of multi-resolution image data for mangrove leaf area index mapping. *Remote Sens. Environ.* **176**, 242–254 (2016).
45. Xiao, J. et al. Remote sensing of the terrestrial carbon cycle: a review of advances over 50 years. *Remote Sens. Environ.* **233**, 111383 (2019).
46. Hawman, P. A., Mishra, D. R. & O'Connell, J. L. Dynamic emergent leaf area in tidal wetlands: implications for satellite-derived regional and global blue carbon estimates. *Remote Sens. Environ.* **290**, 113553 (2023).
47. Justice, C. O. et al. An overview of MODIS Land data processing and product status. *Remote Sens. Environ.* **83**, 3–15 (2002).
48. Tang, Y. et al. Mango-GPP: a process-based model for simulating gross primary productivity of mangrove ecosystems. *J. Adv. Model. Earth Syst.* **15**, e2023MS003714 (2023).

49. Gou, R. et al. Atmospheric water demand constrains net ecosystem production in subtropical mangrove forests. *J. Hydrol.* **630**, 130651 (2024).
50. Vicente-Serrano, S. M., Beguería, S. & López-Moreno, J. I. A multiscalar drought index sensitive to global warming: the Standardized Precipitation Evapotranspiration Index. *J. Clim.* **23**, 1696–1718 (2010).
51. Rienecker, M. M. et al. MERRA: NASA's Modern-Era Retrospective Analysis for Research and Applications. *J. Clim.* **24**, 3624–3648 (2011).
52. Beguería, S., Vicente-Serrano, S. M. & Angulo-Martínez, M. A multiscalar global drought dataset: the SPEIbase: a new gridded product for the analysis of drought variability and impacts. *Bull. Am. Meteorol. Soc.* **91**, 1351–1356 (2010).
53. Guinehut, S., Dhomps, A.-L., Larnicol, G. & Le Traon, P.-Y. High resolution 3-D temperature and salinity fields derived from in situ and satellite observations. *Ocean Sci.* **8**, 845–857 (2012).
54. Rovai, A. S. et al. Macroecological patterns of forest structure and allometric scaling in mangrove forests. *Glob. Ecol. Biogeogr.* **30**, 1000–1013 (2021).
55. Almar, R. et al. Influence of El Niño on the variability of global shoreline position. *Nat. Commun.* **14**, 3133 (2023).
56. Yan, R. et al. Interactive effects of the El Niño–Southern Oscillation and Indian Ocean Dipole on the tropical net ecosystem productivity. *Agric. Meteorol.* **336**, 109472 (2023).
57. Enríquez, A. R. et al. Predictable changes in extreme sea levels and coastal flood risk due to long-term tidal cycles. *J. Geophys. Res. Oceans* **127**, e2021JC018157 (2022).
58. Peng, D., Hill, E. M., Meltzner, A. J. & Switzer, A. D. Tide gauge records show that the 18.61-year nodal tidal cycle can change high water levels by up to 30 cm. *J. Geophys. Res. Oceans* **124**, 736–749 (2019).
59. Chen, C., Riley, W. J., Prentice, I. C. & Keenan, T. F. CO_2 fertilization of terrestrial photosynthesis inferred from site to global scales. *Proc. Natl Acad. Sci. USA* **119**, e2115627119 (2022).
60. Kim, J.-S., Kug, J.-S. & Jeong, S.-J. Intensification of terrestrial carbon cycle related to El Niño–Southern Oscillation under greenhouse warming. *Nat. Commun.* **8**, 1674 (2017).
61. Bunting, P. et al. Global Mangrove Watch (1996–2020) version 3.0 dataset. *Zenodo* https://doi.org/10.5281/zenodo.6894273 (2022).
62. Duke, N. C., Ball, M. C. & Ellison, J. C. Factors influencing biodiversity and distributional gradients in mangroves. *Glob. Ecol. Biogeogr. Lett.* **7**, 27–47 (1998).

Acknowledgements

Y.L. acknowledges the support from the National Natural Science Foundation of China Grants (grant no. 42276232). D.F. thanks M. and M. Cochran for endowing the Cochran Family Professorship in Earth and Environmental Sciences at Tulane University. We thank W. Cai at the Commonwealth Scientific and Industrial Research Organisation (CSIRO) for his feedback on an earlier version of this work.

Author contributions

Z.Z. conceptualized the study. Z.Z. and Y.L. designed the study. Z.Z. performed the analysis and drafted the paper with contributions from all other co-authors. All authors contributed to the interpretation of the results. Y.L. is the main corresponding author of the study.

Competing interests

The authors declare no competing interests.

Additional information

Extended data is available for this paper at https://doi.org/10.1038/s41561-025-01701-8.

Supplementary information The online version contains supplementary material available at https://doi.org/10.1038/s41561-025-01701-8.

Correspondence and requests for materials should be addressed to Zhen Zhang or Yangfan Li.

Peer review information *Nature Geoscience* thanks Norman Duke, Melinda Martinez and the other, anonymous, reviewer(s) for their contribution to the peer review of this work. Primary Handling Editor: Xujia Jiang, in collaboration with the *Nature Geoscience* team.

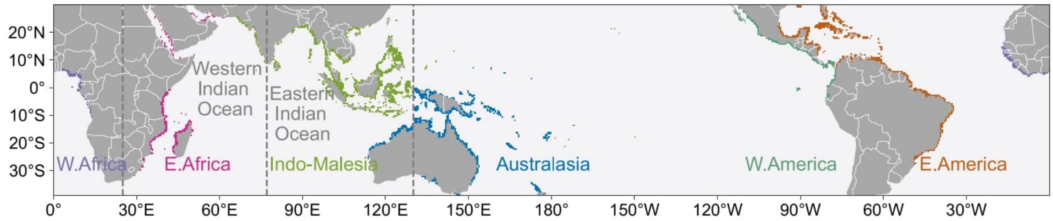

Extended Data Fig. 1 | Distribution of mangroves within six biogeographic regions. This map was adopted from ref. 62.

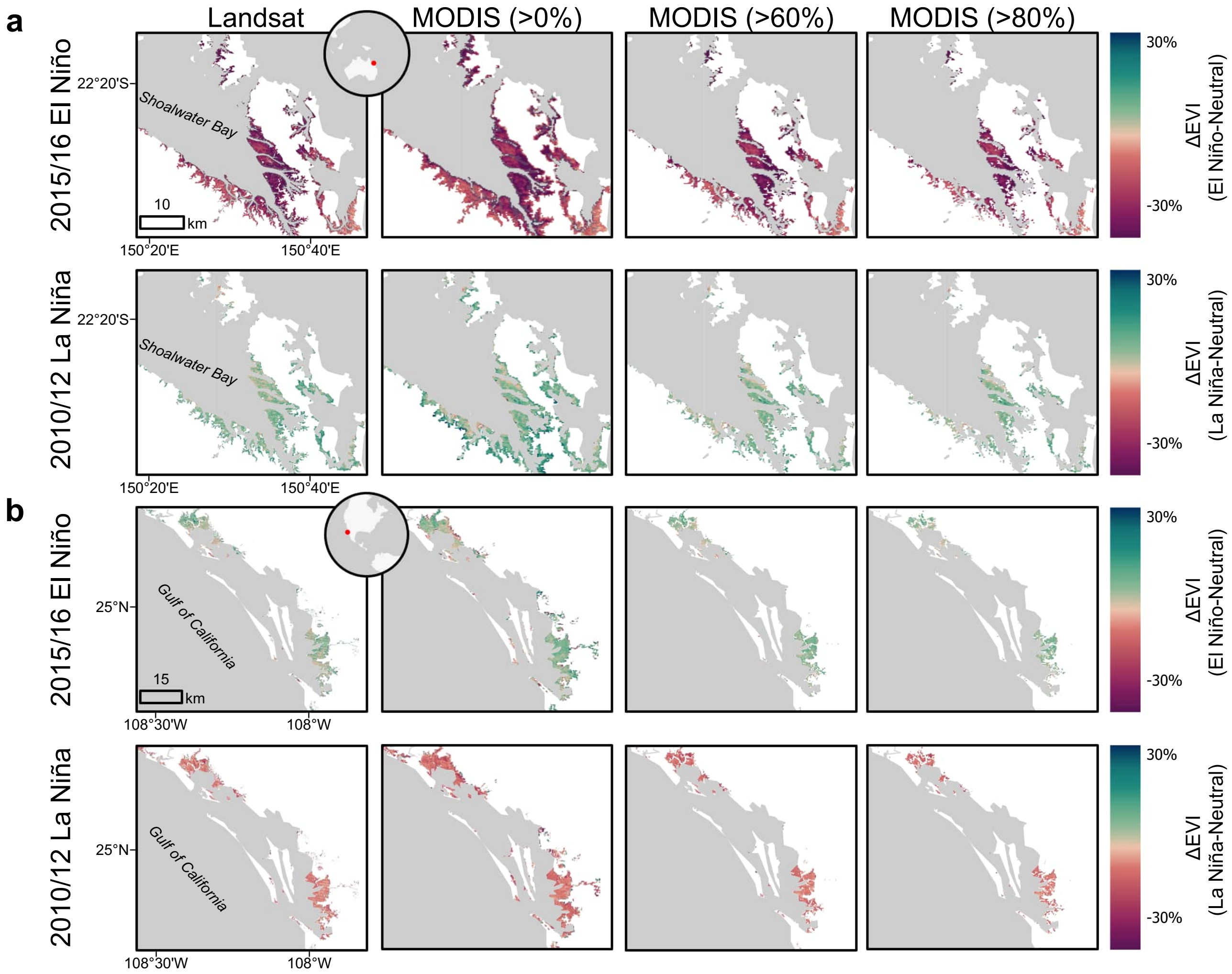

Extended Data Fig. 2 | Local-scale mangrove variation in response to ENSO. ΔEVI (average EVI during ENSO event minus average EVI during neutral periods) in (**a**) Shoalwater Bay, Australia, and (**b**) Gulf of California, Mexico. The left panels show Landsat results at 30-m resolution. The other three-column panels show MODIS results at 250-m resolution with three different criteria to define mangrove extents. The right panels show results for pure mangrove pixels (mangrove coverage > 80%) at 250-m resolution, which is used in the main analysis. Areas with green color represent mangroves with enhanced growth, and red color indicates mangrove degradation during the ENSO event.

https://doi.org/10.1038/s41561-025-01701-8

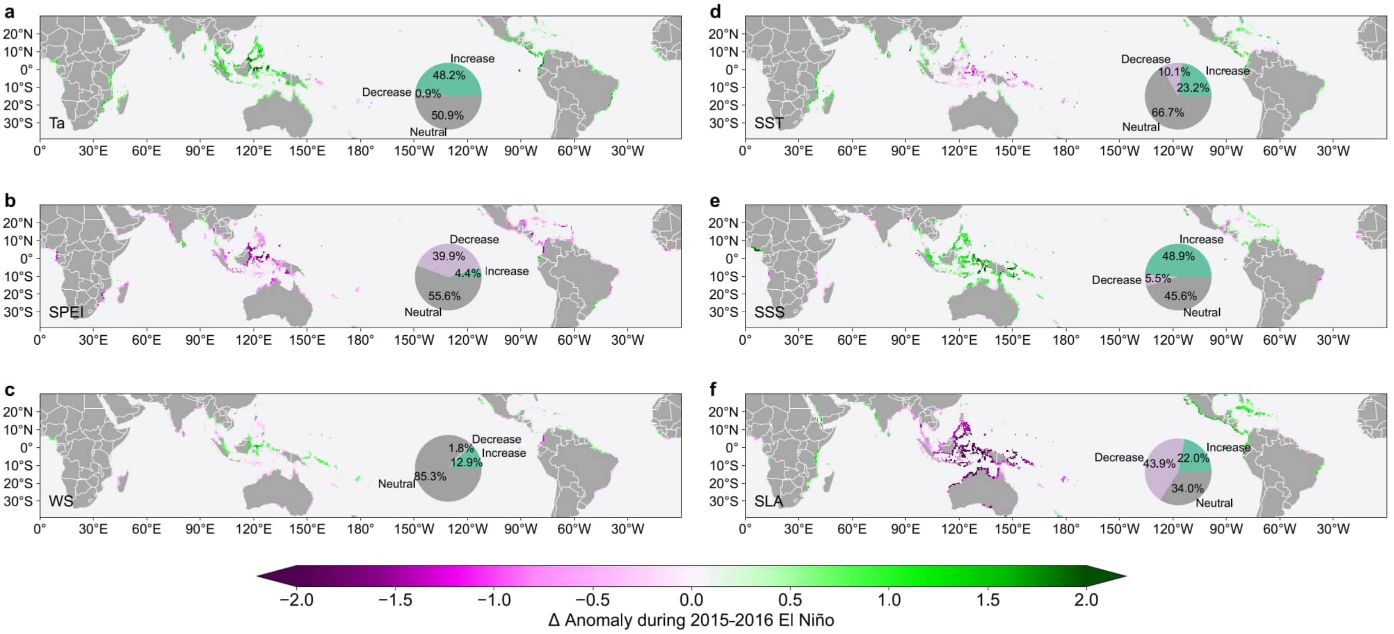

Extended Data Fig. 3 | Observed spatial patterns of changes in climatic and oceanic factors corresponding to 2015-2016 El Niño. Changes in anomaly (z-score) of mean monthly (**a**) air temperature, (**b**) SPEI, (**c**) wind speed, (**d**) sea surface temperature, (**e**) sea surface salinity, and (**f**) sea-level anomaly are shown. Pie plots indicate the area-weighted proportion of grid cells with significantly increased LAI (green), significantly decreased LAI (purple), or no significant difference with neutral phases (grey) ($P > 0.05$).

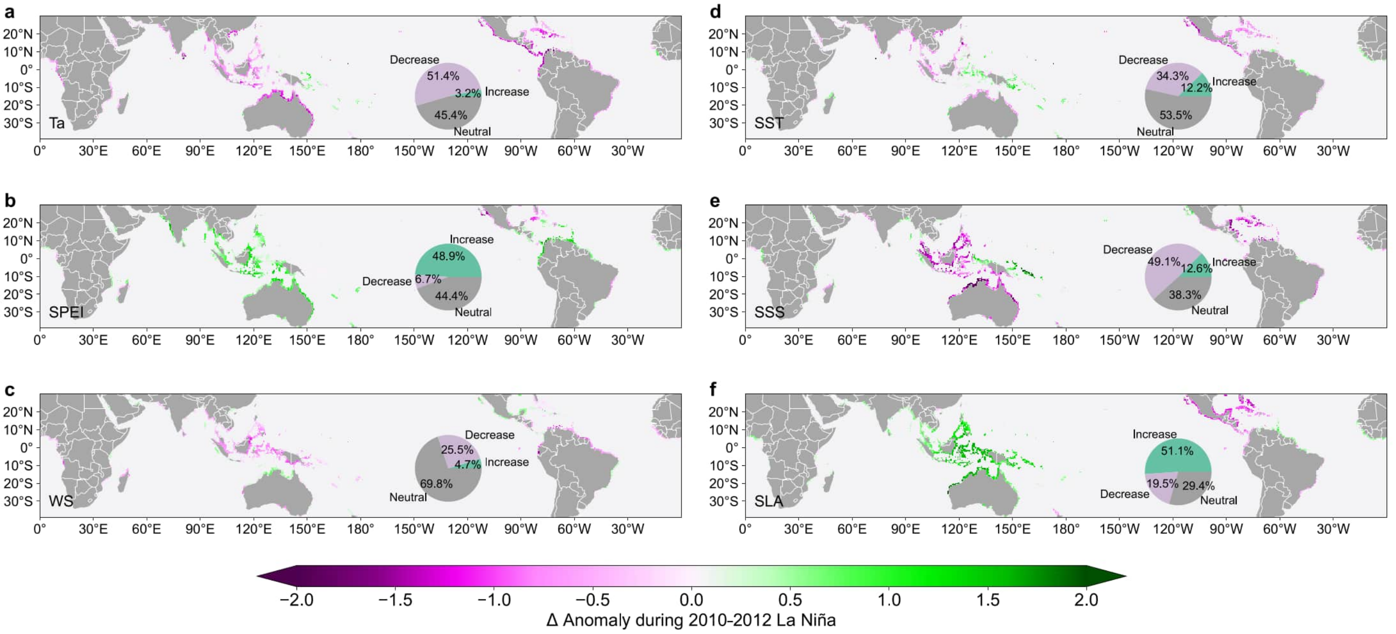

Extended Data Fig. 4 | Observed spatial patterns of changes in climatic and oceanic factors corresponding to 2010-2012 La Niña. Changes in anomaly (z-score) of mean monthly (**a**) air temperature, (**b**) SPEI, (**c**) wind speed, (**d**) sea surface temperature, (**e**) sea surface salinity, and (**f**) sea-level anomaly are shown. Pie plots indicate the area-weighted proportion of grid cells with significantly increased LAI (green), significantly decreased LAI (purple), or no significant difference with neutral phases (grey) ($P > 0.05$).

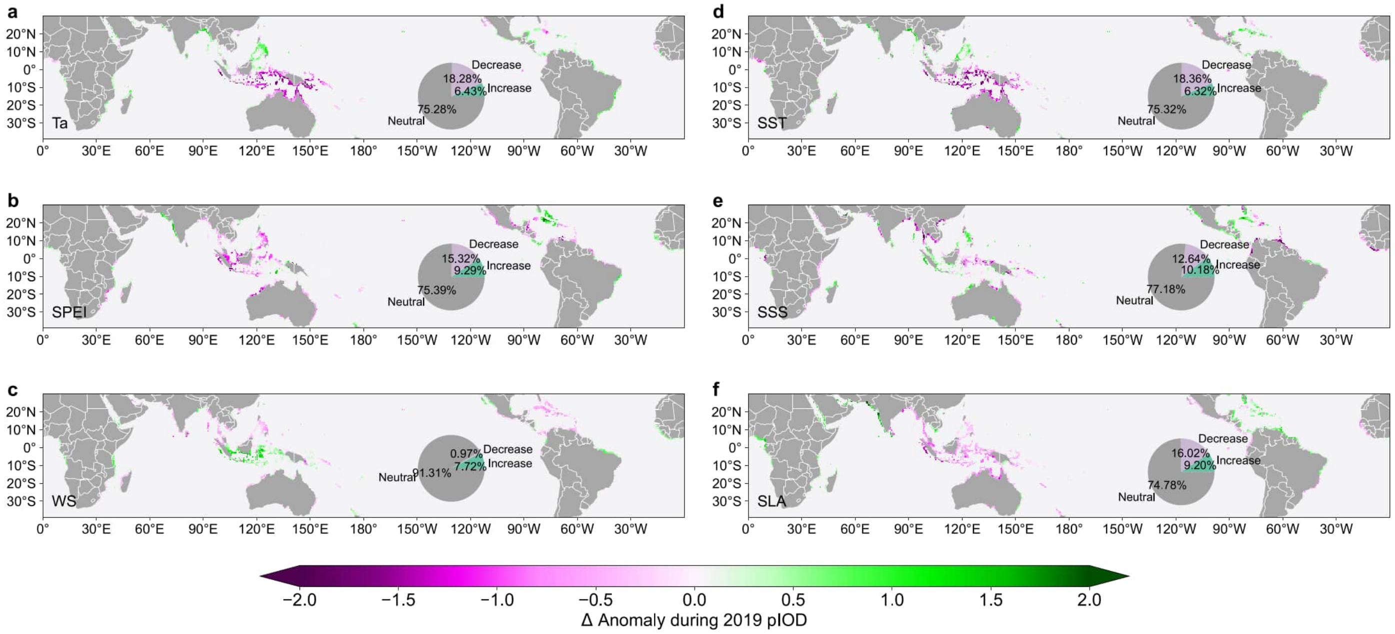

Extended Data Fig. 5 | Observed spatial patterns of changes in climatic and oceanic factors corresponding to 2019 pIOD. Changes in anomaly (z-score) of mean monthly (**a**) air temperature, (**b**) SPEI, (**c**) wind speed, (**d**) sea surface temperature, (**e**) sea surface salinity, and (**f**) sea-level anomaly are shown. Pie plots indicate the area-weighted proportion of grid cells with significantly increased LAI (green), significantly decreased LAI (purple), or no significant difference with neutral phases (grey) ($P > 0.05$).

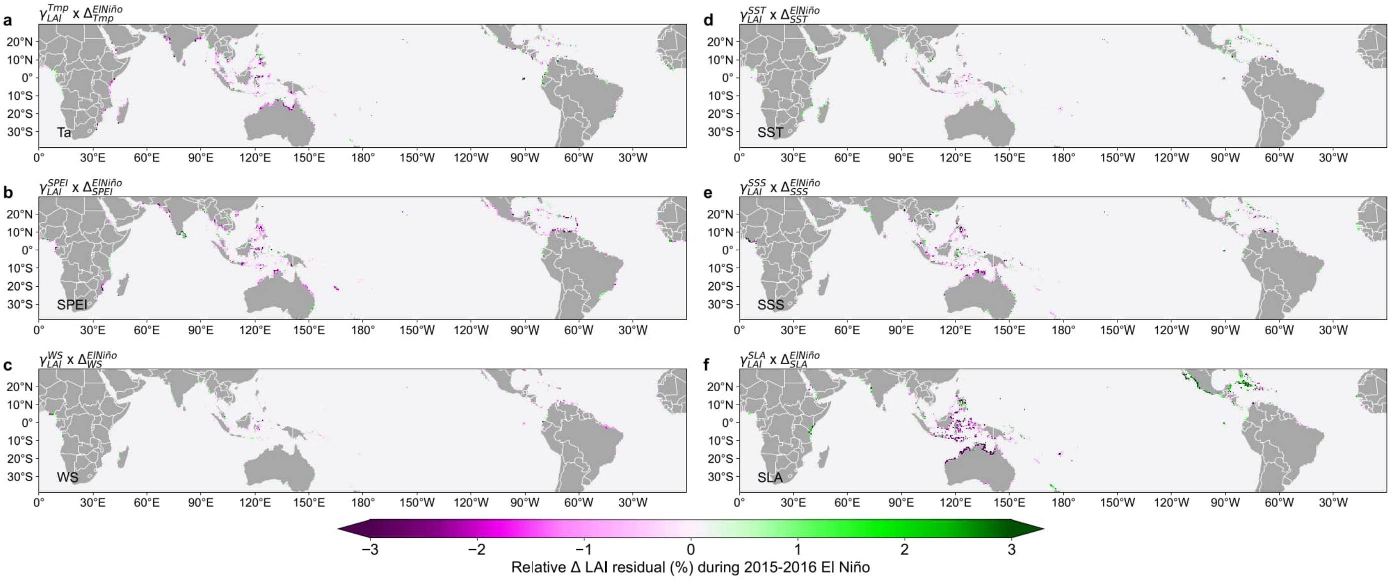

Extended Data Fig. 6 | Each term in Eq. (4) plotted as a contribution to ΔLAI anomaly in the response to 2015-2016 El Niño. The contribution is calculated as the product of mangrove sensitivity to (**a**) air temperature, (**b**) SPEI, (**c**) wind speed, (**d**) sea surface temperature, (**e**) sea surface salinity, and (**f**) sea-level anomaly and El Niño-induced anomaly in these factors.

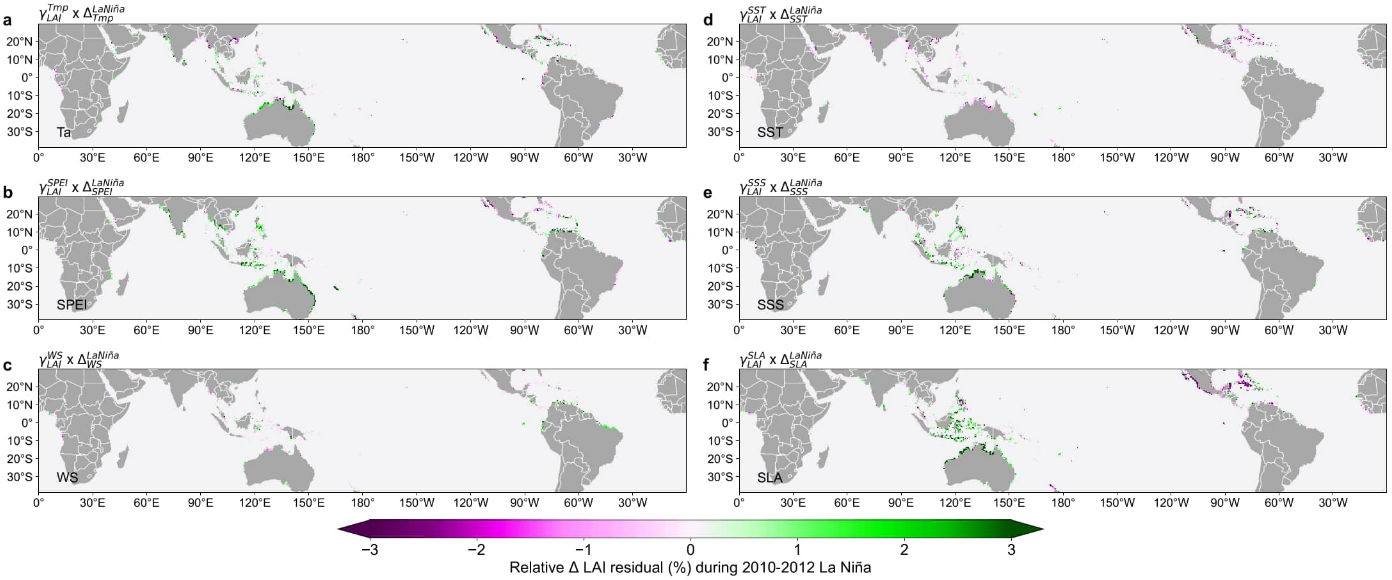

Extended Data Fig. 7 | Each term in Eq. (4) plotted as a contribution to ΔLAI anomaly in the response to 2010-2012 La Niña. The contribution is calculated as the product of mangrove sensitivity to (**a**) air temperature, (**b**) SPEI, (**c**) wind speed, (**d**) sea surface temperature, (**e**) sea surface salinity, and (**f**) sea-level anomaly and La Niña-induced anomaly in these factors.

https://doi.org/10.1038/s41561-025-01701-8

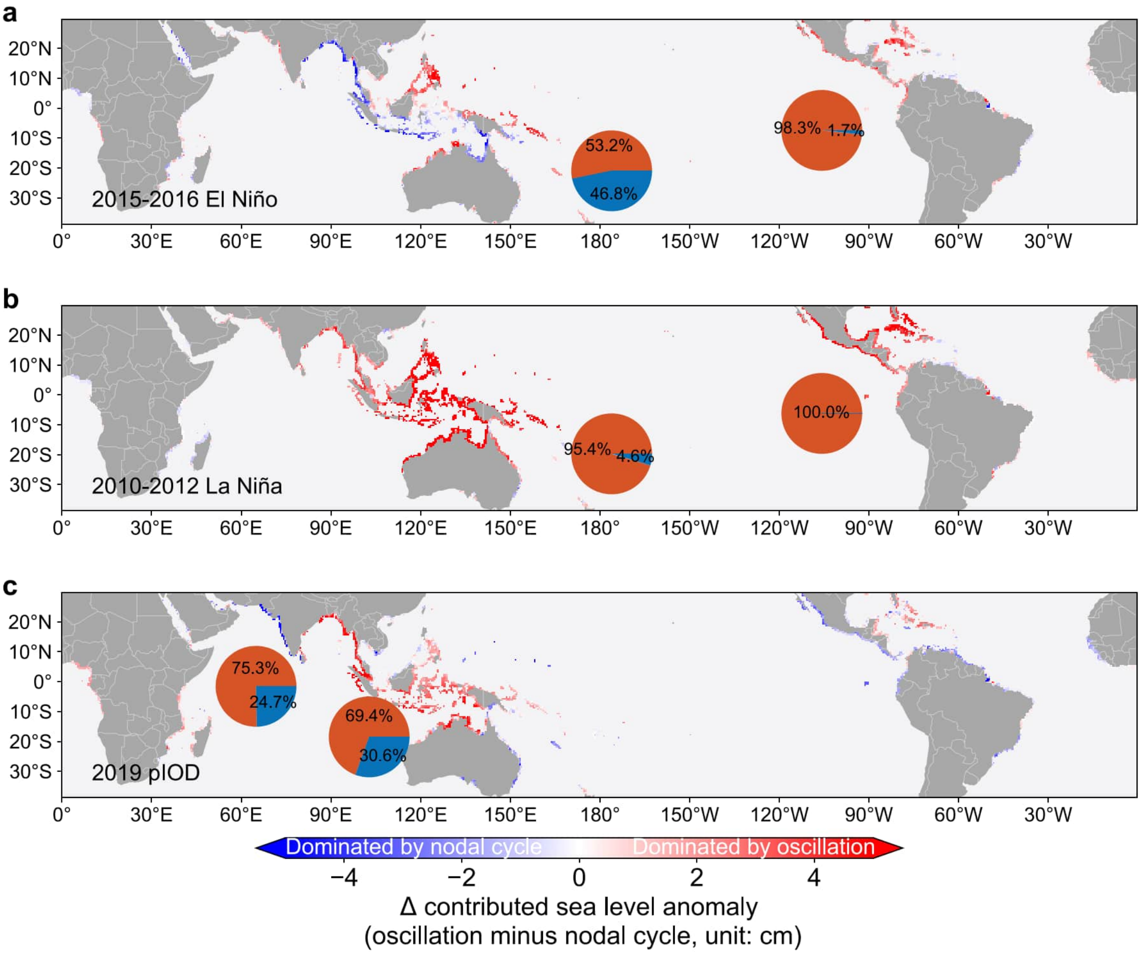

Extended Data Fig. 8 | Dominant driver of sea level anomaly during climatic events. The dominant component driving SLA during (**a**) 2015-2016 El Niño, (**b**) 2010-2012 La Niña, and (**c**) 2019 pIOD. In (**a**) and (**b**), the left pie charts represent results from Indo-Malesia and Australasia, while in (**c**), the left pie chart shows results from eastern Africa. The right pie charts in (**a**) and (**b**) depict results from western America, while in (**c**), the right pie chart shows results from Indo-Malesia and Australasia. The red areas in the charts denote regions where SLA is predominantly influenced by climatic oscillations, and the blue areas indicate regions where the nodal cycle is the dominant factor. Specific spatial details of SLA contributed by climatic oscillations and nodal cycle are shown in Supplementary Fig. 8.

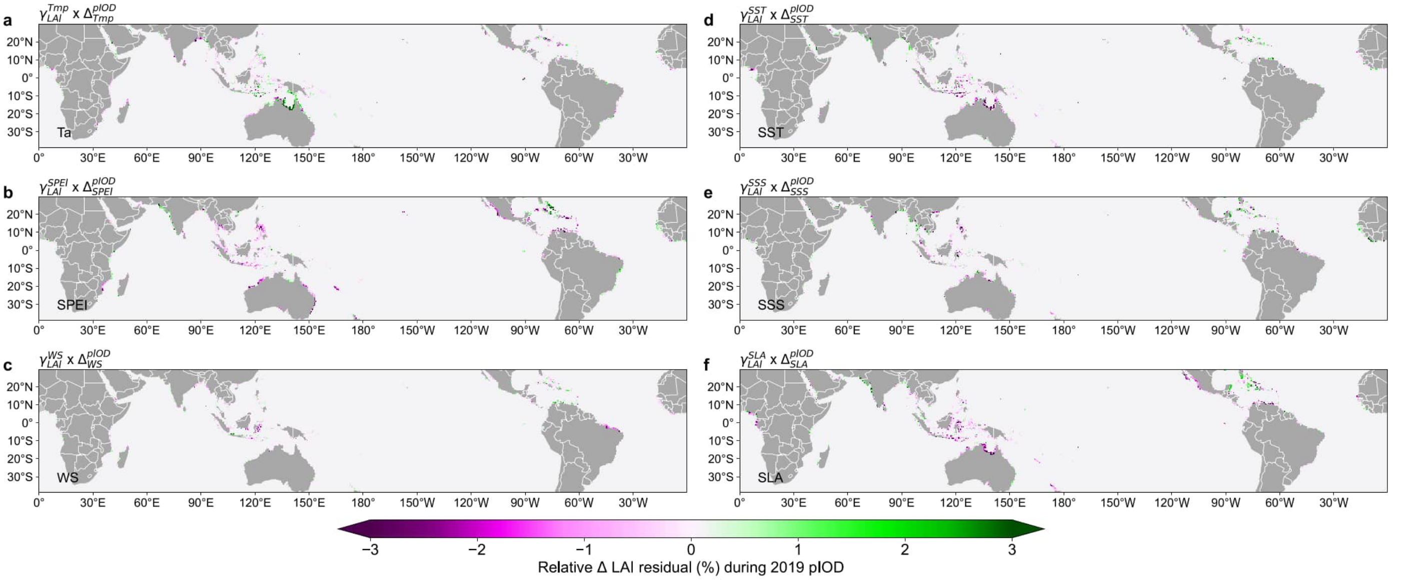

Extended Data Fig. 9 | Each term in Eq. (4) plotted as a contribution to ΔLAI anomaly in the response to 2019 pIOD. The contribution is calculated as the product of mangrove sensitivity to (**a**) air temperature, (**b**) SPEI, (**c**) wind speed, (**d**) sea surface temperature, (**e**) sea surface salinity, and (**f**) sea-level anomaly and pIOD-induced anomaly in these factors.